

Xin Dong

Department of Mechanical,
Materials and Manufacturing Engineering,
University of Nottingham,
C31 Coates Building,
University Park,
Nottingham NG7 2RD, UK

Mark Raffles

Department of Mechanical,
Materials and Manufacturing Engineering,
University of Nottingham,
Manufacturing Building,
University Park,
Nottingham NG7 2RD, UK

Salvador Cobos-Guzman

Department of Mechanical,
Materials and Manufacturing Engineering,
University of Nottingham,
Manufacturing Building,
University Park,
Nottingham NG7 2RD, UK

Dragos Axinte¹

Department of Mechanical,
Materials and Manufacturing Engineering,
University of Nottingham,
A63 Coates Building,
University Park,
Nottingham NG7 2RD, UK
e-mail: Dragos.Axinte@nottingham.ac.uk

James Kell

Repair Technology,
Rolls-Royce plc,
Derby DE24 8BJ, UK

A Novel Continuum Robot Using Twin-Pivot Compliant Joints: Design, Modeling, and Validation

A twisting problem is identified from the central located flexible backbone continuum robot. Regarding this problem, a design solution is required to mechanically minimize this twisting angle along the backbone. Further, the error caused by the kinematic assumption of previous works is identified as well, which requires a kinematic solution to minimize. The scope of this paper is to introduce, describe and teste a novel design of continuum robot which has a twin-pivot compliant joint construction that minimizes the twisting around its axis. A kinematics model is introduced which can be applied to a wide range of twin-pivot construction with two pairs of cables per section design. And according to this model, the approach for minimising the kinematic error is developed. Furthermore, based on the geometry and material property of compliant joint, the work volumes for single/three-section continuum robot are presented, respectively. The kinematic analysis has been verified by a three-section prototype of continuum robot and adequate accuracy and repeatability tests carried out. And in the test, the system generates relatively small twisting angles when a range of end loads is applied at the end of the arm. Utilising the concept presented in this paper, it is possible to develop a continuum robot which can minimize the twisting angle and be accurately controlled. In this paper, a novel design of continuum robot which has a twin-pivot compliant joint construction that minimizes the twisting around its axis is introduced, described and tested. A kinematics model is introduced which can be applied to a wide range of twin-pivot construction with two pairs of cables per section design. Furthermore, based on the geometry and material property of compliant joint, the work volumes for single/three-section continuum robot are presented, respectively. Finally, the kinematic analysis has been verified by a three-section prototype of continuum and adequate accuracy and repeatability tests carried out.

[DOI: 10.1115/1.4031340]

Introduction

Continuum robots, unlike traditional rigid-link designs, feature a continuous shape with multisection construction. Due to their unique flexibility, continuum robots can reach places that are usually inaccessible for rigidlike robot and hostile for human beings. A wide range of applications have been demonstrated in the medical field as minimally invasive surgery robot and endoscopes [1–9]. Further, the potential applications include navigation and operation in confined environments, such as rescues in collapsed buildings or military detection [10–12].

However, some challenges remain in the design of continuum robots. The flexibility of continuum robots determines the obstacle avoidance capability of the system. For rigid backbone continuum robots, the flexibility is determined by the number of joints (universal or spherical joints) in a single section. Due to the degrees of freedom (DOF) of a single section (2DOF), rigid backbone continuum robots can only employ one universal joint (2DOF) in each section [13,14]. The solution for employing multi-rigid joints in single section is to utilize springs [15,16] or other elastic material (Teflon flexure/rubber) [4] to make all these joints have the same stiffness so that they can bend evenly, when the section is bent; nevertheless, these designs cause the continuum robot to be bulky/low bending stiffness, which makes it difficult

to access confined workplaces/carry appropriate weight end effector. For flexible backbone robots, due to the elastic property, the whole backbone performs as an elastic universal joint, resulting in continuous bending of continuum robot. Therefore, it allows the continuum robots to be designed light-weight and small size [5–7,17,18], thus having great obstacle avoidance capability in narrow environment. However, the long flexible backbone leads to low stiffness and hence, low position accuracy. Therefore, a design solution is needed to be developed to provide great flexibility and stiffness simultaneously. Furthermore, the system with a central located flexible backbone has great flexibility, but it results parasitic twists around the length when the robot bends in the horizontal plane; this could result in difficulties in the kinematic modeling and control. Nevertheless, to the best of author's knowledge, at the moment, there is no specific information presented for addressing this problem in terms of design. Unlike the flexible backbone, some other designs employ the compliance of flexible beams arranged in a planar plane as the bending resource [19,20]. The constructions demonstrate good capabilities of flexibility. However, this arrangement makes it difficult to estimate/control the backbone length, since the varying actuation force along the longitude direction compress the backbone to variable lengths in the process of operation.

Significant efforts in the area have been focused on the kinematics of the continuum robots [21,22]. Jones and Walker presented a geometrical method for deriving the kinematics by assuming the robot bends as a constant curvature [22]. Furthermore, Simaan utilizes the same assumption for solving the

¹Corresponding author.

Manuscript received February 16, 2015; final manuscript received July 14, 2015; published online November 24, 2015. Assoc. Editor: Byung-Ju Yi.

kinematics of a minimally invasive surgery continuum robot [23]. Webster and Jones presented a review from a wide range of publications covering kinematic modeling of constant curvature continuum robots [24]. However, it seems that the kinematics of the continuum robots presented in these reports assume the section bending angle is equal to tip disk orientation angle with respect to the base disk of the section. However, as it proved later in the paper it is not a comprehensive assumption as there is a difference (max. 4–10 deg for 90 deg bend) between these two angles, which causes an error for inverse kinematics (see New Concept of Novel Continuum Robot Design, for details).

In this paper, we present a novel continuum design, which has a twin-pivot compliant joint construction; thus, the stiffness can be significantly increased and the parasitic twist minimized which is a general drawback of the flexible backbone continuum robots. Further, regarding the proposed design solution and kinematic error (see New Concept of Novel Continuum Robot Design, for details), a kinematic model of the cable-actuation system is presented, which can minimize the position error. Furthermore, the kinematic model is modular, allowing its application to a wide range of twin-pivot construction with two pairs of cables per section design. Next, the cable tension is also calculated for proving the cables can be kept in tension in any configuration. The work volume of this robot is presented based on the proposed design. Finally, the control accuracy, repeatability, motion range, twisting angle and load carrying capability of the system are validated by the experiment on the physical demonstrator.

New Concept of Novel Continuum Robot Design

In general, continuum robots consist of a backbone (to support the structure and enable the bending movement), joints (to allow the bending movement), disks (to constrain the cables) and cables (to actuate the construction and keep the stiffness of the system). According to the backbone design, the continuum robots can be classified into two groups. One utilizes a rigid backbone connected by single/multi universal joints in one section, while others employ flexible rod/tubes as backbone, which are made of materials capable to take high elastic displacements, such as super-elastic NiTi or rubber.

Disadvantages and Challenge of the Existing Continuum Robots

(1) *Twist Problem.* Compared with rigid backbone continuum robots, the flexible backbone design has good flexibility and small diameter/length ratio making them more suitable for operating in tight environment. However, the flexible backbone of the arm is twisted along its length due to the torque generated by the weight of the system and the payload, as shown in Fig. 1. Only the bend movement about Y and Z axes (2DOF), as shown in Fig. 1, can be controlled by the actuators in single section, as a result, the twist angle about X axis cannot be controlled, which makes difficult in kinematic modeling and control.

The twisting angle of segment backbone (without cables constraint) can be expressed as

$$\phi = \frac{TL}{GI_x} \quad (1)$$

Where T is the twisting torque; L is the length of the flexible backbone; I_x is the moment of inertia; G is the shear modulus of elasticity, which can be written as $G = E/2(1 + \nu)$; E is elastic modulus; ν is Poisson's ratio.

For example, let assume the super-elastic NiTi rod (length of a single segment, $L = 15$ mm; diameter = 1 mm) on which a torque $T = 0.1$ Nm is applied at its end, refer to Eq. (33), the twisting angle $\phi = 58.22$ deg. (The twisting angles are not constant against different payloads and configurations). For decreasing the twisting angle, one solution is to apply more force along the cables, but it will accuse the buckling of the flexible backbone if the force along

the backbone exceeds the buckling load. Therefore, the better solution in such instance is to design the backbone which can mechanically minimize the twisting angle.

(2) *Kinematic challenge.* The purpose of inverse kinematics is to determine the lengths of actuating cables for a known position of the robot tip in order to control the shape of the continuum robot. According to the tool center point (TCP) of section (X_p , Y_p and Z_p), the section bending and directional angles are expressed in terms of X_p , Y_p and Z_p . In the previous work [10,21–23], for inverse kinematic analysis, section bending angle is considered being equal with the tip disk orientation angle with respect to the base disk for simplifying the calculation.

For flexible backbone/multi universal-joint continuum robot, these two angles do not couple with each other, as shown in Fig. 2(b), unless the thickness of the disk is infinitesimal small. In other words, the bending angles of section and tip disk will be equal, only when the backbone is purely continuous along the whole length, as shown in Fig. 2(a). This simplification can cause an error for continuum robot position control, but to date, there is limited information reported on addressing this problem.

Figure 3 shows a case study for calculating the angle difference with these two angles in work volume of single section continuum robot (max. 8 deg).

New Design Concept for Continuum Robot Construction (Twin-Pivot Compliant Joint). To overcome the aforementioned disadvantages, especially the twisting problem, a novel design of a continuum robot is presented, which provides improved flexibility and eliminates the twist problem while employing two actuators for each section.

As shown in Fig. 4(a), the continuum robot consists of disks, actuation cables and twin-pivot compliant joints. The disks are connected by compliant joints; the continuum robot bend is caused by the torque generated through actuation cables. Figures 4(b) and 4(c) show the twin-pivot compliant joint construction of a continuum robot which consists of the following elements:

Compliant Joint (rod/tube/sheet) is made of a material which is flexible and able to be bent with little residual plastic deformation (e.g., super-elastic Nitinol). As shown in Fig. 4(b), two rods/tubes are located in plane A-A; and the other two are located in plane B-B. The angle θ is 90 deg. So arbitrary direction (2DOF) bend can be generated.

Disks are utilized for constraining the cables; Cables consist of two pairs of cables, each being actuated by a single motor.

Based on this design, a novel continuum robot can carry an appropriate payload with a twin actuation design, while giving the possibility to be constructed with a small diameter/length ratio, great flexibility and minimized twisting, so that it can access confined spaces thus be applicable for a variety of machining and visual inspection tasks.

System Overview

For validating the twin-pivot compliant joint concept, a high-dexterity three-section continuum demonstrator (Fig. 5) was designed and built, which employs twin actuation per section. Note that in the following the main emphasis on the design aspect is given to the continuum unit.

Figure 5 presents a demonstrator of a three sections (each section contains ten segments) continuum system. Each segment is 10 mm long and composed of two pairs of cables (locked/attached that the end of each section), three disks (lower, middle and upper) and the disks are connected by double 1.5 mm long, 1 mm diameter super-elastic NiTi rods. The whole arm weight is 62 g.

By actively changing the lengths of two out of the four steel cables, each section can be bent at least 90 deg in arbitrary direction. The current design of disks is 15 mm in diameter and pitch circle diameter for cable guide holes is 12 mm. For delivering electrical cables of end-effectors (e.g., camera, cutting tool) to the

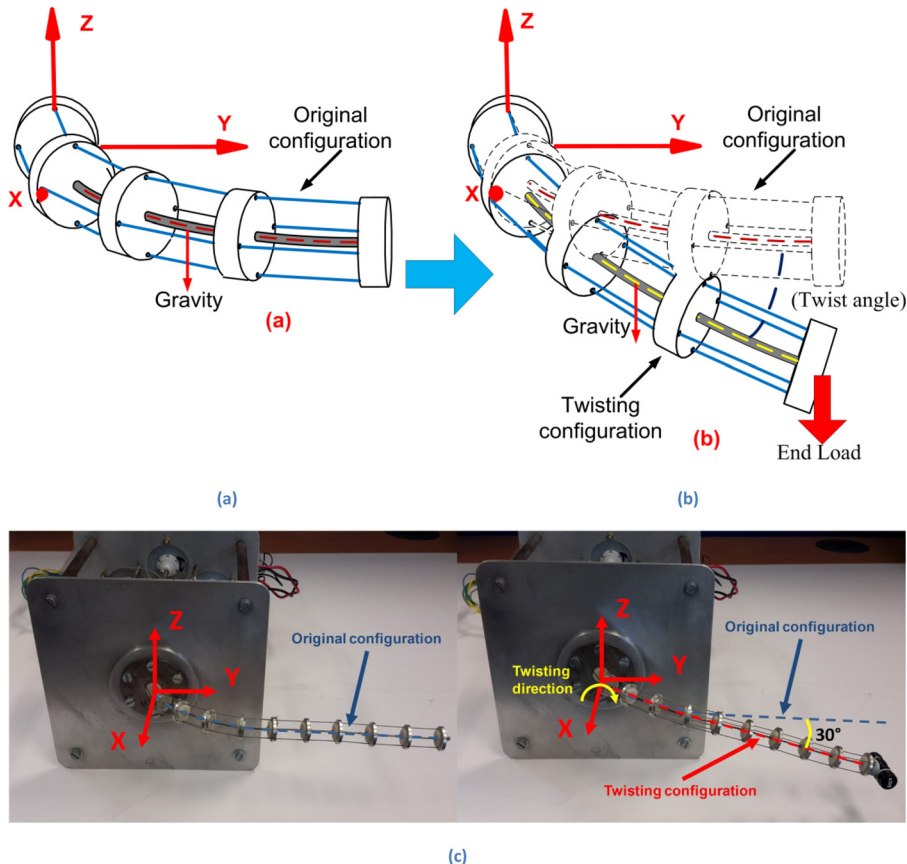


Fig. 1 A schematic representation of the parasitic twist of the continuum robot utilizing the central located flexible backbone design: (a) original configuration (affected by gravity); (b) twisting configuration (affected by gravity + end load); (c) the twisting problem identified from a physical demonstrator (each section is 100 mm in length and 15 mm in diameter; the diameter of the NiTi backbone is 1 mm; the end load is 20 g and the twisting angle is 30 deg)

tip of the robot, a 9 mm diameter hole is made in the center of each disk, hence over the entire length of the continuum unit.

Most reported cable-driven continuum robots employ three actuators or two actuators with complex cable tension mechanism for each section [4,26].

Figure 6 shows a concept of two pairs of cables design using a compact spool mechanism. In this section, an actuation mechanism is proposed which can mechanically keep the cable tension, and achieves a proportional relationship between actuator motion and manipulator motion.

Figure 7 shows the specific design of the spool mechanism employed in the continuum robot system. The cables are helically coiled on the spool. Thus, the same cable length can be fed in and pulled out from both sides by the rotation of the motor, which renders the tension of cables can be maintained at any configuration (see cable tension analysis for details).

Kinematic Analysis

As commented, the kinematics of continuum robots has been previously commented. However, due to a unique twin-pivot construction utilized in this system and the kinematic error that this new design intends to minimize, the kinematics of the system needs to be discussed in detail. Firstly, a model is presented for computing the kinematics of the continuum robot, which assumes that the compliant joint performs as an arc of circle, as shown in Fig. 8; follow-up experiments indicate that this assumption is reasonable. Further, the desired length of one pair of cables at arbitrary configuration is calculated and compared to real length (constant value, fixed after cable fully tensioned) to

prove the cable can keep tension well based on the twin actuation design.

Forward Kinematics. The purpose of forward kinematic analysis is to determine the tip position of the continuum robot with given lengths of cables. As each section includes identical segments, the forward kinematic model is expressed, based on the analysis of a single segment (Fig. 9) on which the compliant joint is assumed to perform as a pure arc.

TCP position and orientation of single section is derived via Denavit–Hartenberg (DH) method, after obtaining DH parameters (β_1 and β_2) with given cable lengths (l_1 and l_2). Step A: based on l_1 and l_2 , find the bending angles β_1 and β_2 . As shown in Fig. 8(a), the difference between l'_1 and l'_3 can be obtained, due to the length of one pair of cables in one gap is constant to $2l_{\text{joint}}$ (the compliant joint in this system is short, (1.5 mm) and bending angle of each joint is small (up to 9 deg for 90 deg section bend), so the distance between two ends of the joint is extremely close to joint length (0.1% difference).

$$l'_3 - l'_1 = (2 \cdot l_{\text{joint}} - l'_1) - l'_1 \quad (2)$$

Where l_{joint} is given.

As shown in Fig. 8(b), the projection of line B1B3 on joint 1 bending plane can be expressed as

$$m_{B_1B_3} = 2 \cdot r \cdot \sin(\theta_1) \quad (3)$$

Where r and θ_1 are given.

Hence, from joint 1 bending section view, the following equation can be given by:

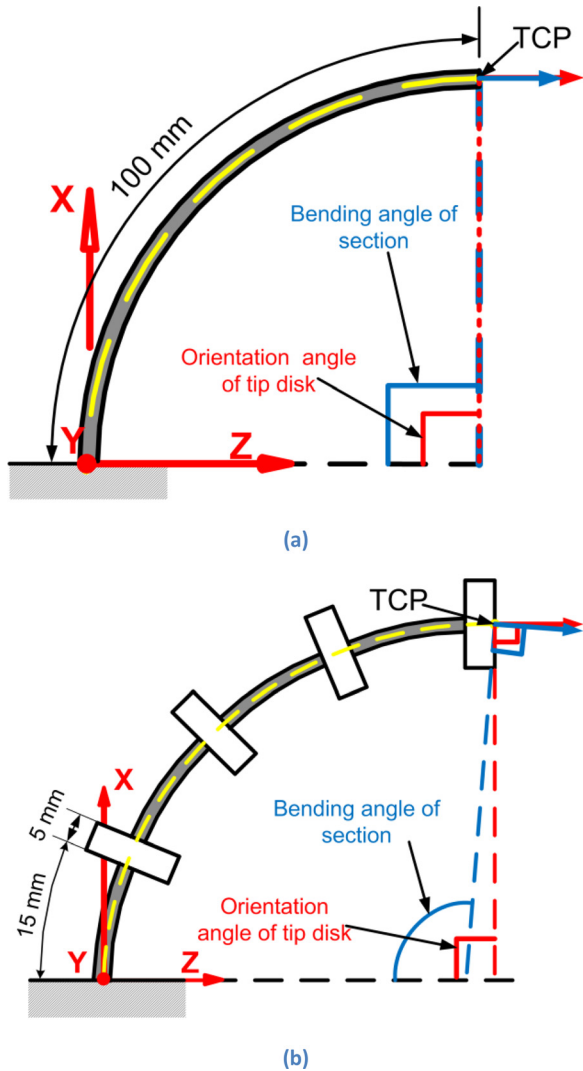


Fig. 2 Schematic showing the difference between section and tip disk bending angles: (a) continuous backbone (represented without the platforms) [25] (b) flexible backbone [6]

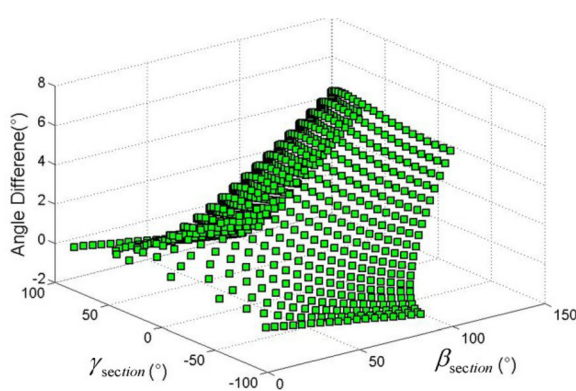


Fig. 3 A plot of the difference between bending angle of section and orientation angle of tip disk (as shown in Fig. 2(b), flexible backbone length and disk thickness are 15 mm and 5 mm, respectively); at 0 deg section bending, the difference is 0 deg. And the max angle difference is 8 deg at section bending angle 90 deg, direction angle 0 deg.

$$(2 \cdot l_{\text{joint}} - l'_1) - l'_1 = 2 \cdot m_{B_1B_3} \cdot \sin(\beta_1/2) \\ = 2 \cdot [2 \cdot r \cdot \sin(\theta_1)] \cdot \sin(\beta_1/2) \quad (4)$$

Similarly, the difference between l'_2 and l'_4 can be obtained

$$(2 \cdot l_{\text{joint}} - l'_2) - l'_2 = 2 \cdot [2 \cdot r \cdot \sin(\pi/2 - \theta_1)] \cdot \sin(\beta_1/2) \quad (5)$$

Likewise, from joint 2 bending section view, another two equations can be obtained

$$(2 \cdot l_{\text{joint}} - l''_1) - l''_1 = 2 \cdot [2 \cdot r \cdot \cos(\theta_1)] \cdot \sin(\beta_2/2) \quad (6)$$

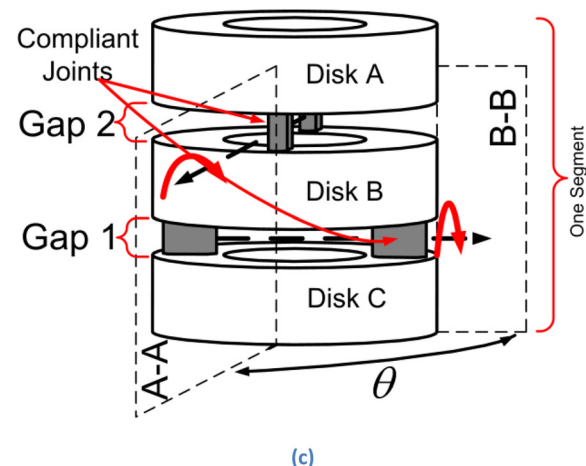
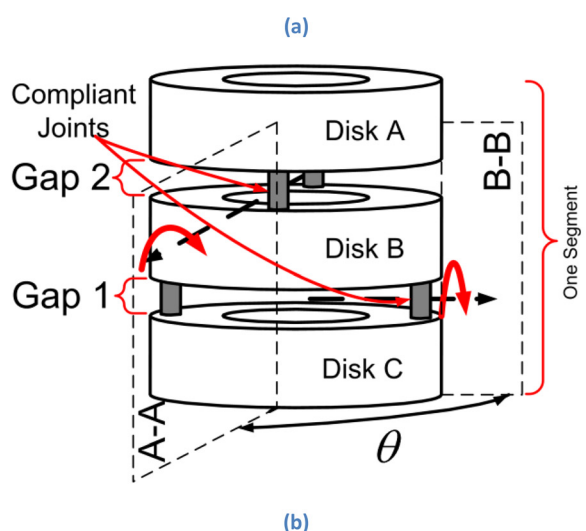
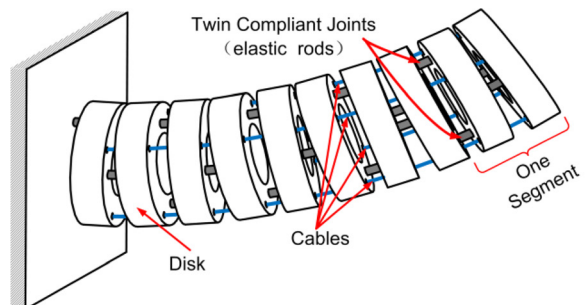


Fig. 4 Continuum robot construction using twin-pivot compliant joints concept: (a) general view of twin-pivot compliant joints robot, (b) one segment of twin-rod concept one, and (c) one segment of twin-sheet concept

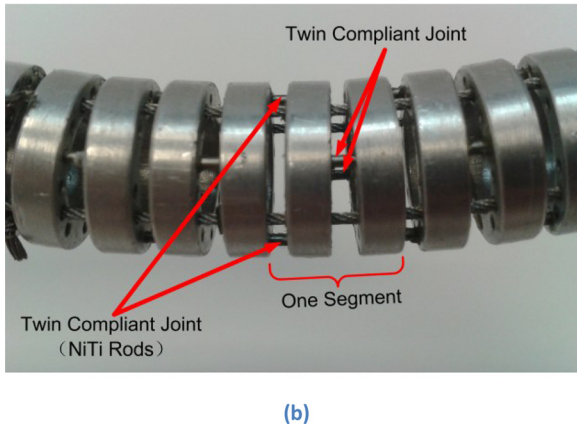
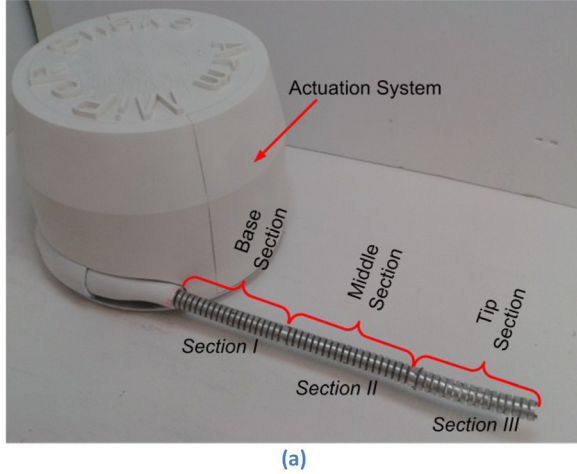


Fig. 5 (a) General view of continuum robot system and (b) one segment construction

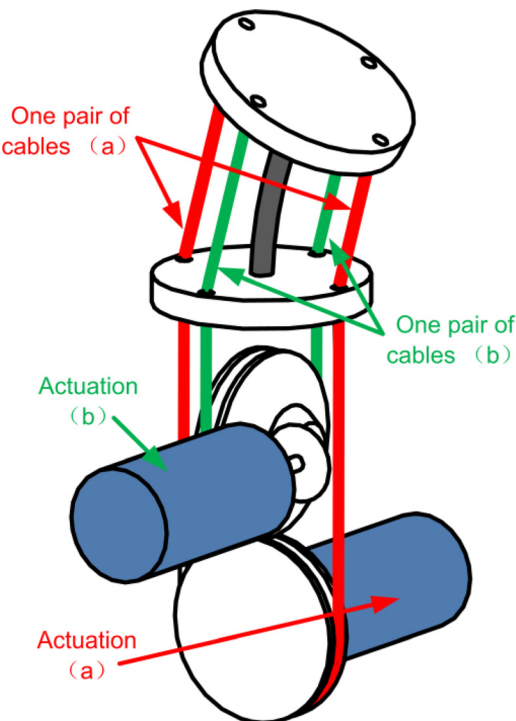


Fig. 6 conceptual schematic of Twin actuation design

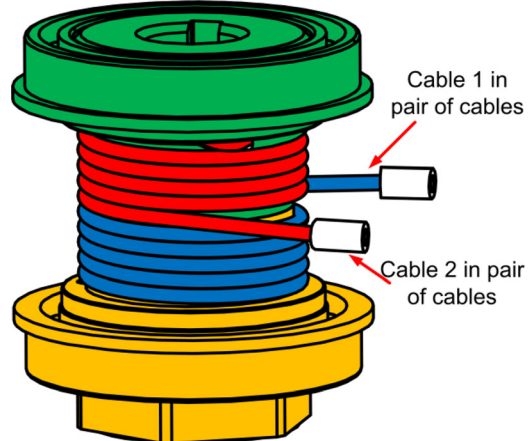


Fig. 7 Spool mechanism

And

$$(2 \cdot l_{\text{joint}} - l_2'') - l_2'' = 2 \cdot [2 \cdot r \cdot \cos(\pi/2 - \theta_1)] \cdot \sin(\beta_2/2) \quad (7)$$

Then, in order to eliminate parameters l_1' and l_1'' , adding the left and right side of Eq. (4) with the left and right sides of Eq. (6), respectively, yields

$$2 \cdot l_{\text{joint}} - l_1 = 2 \cdot r \cdot \sin(\theta_1) \cdot \sin(\beta_1/2) + 2 \cdot r \cdot \cos(\theta_1) \cdot \sin(\beta_2/2) \quad (8)$$

Where l_1 is given.

Likewise, the other equation can be obtained

$$2 \cdot l_{\text{joint}} - l_2 = 2 \cdot r \cdot \cos(\theta_1) \cdot \sin(\beta_1/2) + 2 \cdot r \cdot \sin(\theta_1) \cdot \sin(\beta_2/2) \quad (9)$$

Where l_2 is given.

Based on Eqs. (8) and (9), the bending angles β_1 and β_2 can be written in terms of cable lengths l_1 and l_2 , θ_1 , r and joint length l_{joint} as

$$\begin{cases} \beta_1 = \sin^{-1} \left(\frac{2l_{\text{joint}}(\sin(\theta_1) - \cos(\theta_1)) - l_1 \sin(\theta_1) + l_2 \cos(\theta_1)}{2r(\sin^2(\theta_1) - \cos^2(\theta_1))} \right) \\ \beta_2 = \sin^{-1} \left(\frac{2l_{\text{joint}}(\sin(\theta_1) - \cos(\theta_1)) + l_1 \cos(\theta_1) - l_2 \sin(\theta_1)}{2r(\sin^2(\theta_1) - \cos^2(\theta_1))} \right) \end{cases} \quad (10)$$

Step B: In step A, parameters β_1 and β_2 are derived with given lengths of cables l_1 and l_2 . Hence, as shown in Fig. 10, all D-H parameters are obtained from design and step A, which are shown

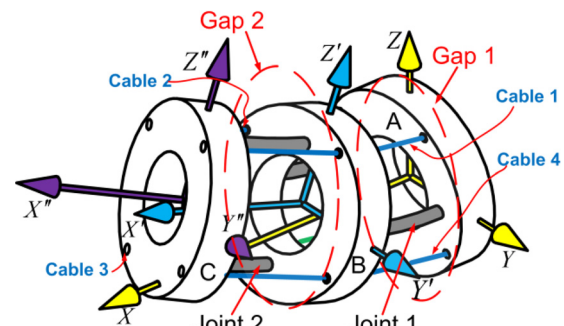


Fig. 8 Schematic for kinematic model of single segment of twin-pivot continuum robot

in Table 1. By using DH method, TCP position and orientation of the section is discussed. As the twin-pivot compliant joint can only bend in a single direction, it is assumed to be bent as a pure curve and performs as a revolute joint.

Using the above D-H table, the matrix for each links can be expressed as, respectively

$$T_0 = \begin{bmatrix} 1 & 0 & 0 & l_{\text{joint}}/\beta_1 \cdot \tan(\beta_1/2) \\ 0 & 1 & 0 & 0 \\ 0 & 0 & 1 & 0 \\ 0 & 0 & 0 & 1 \end{bmatrix} \quad (11)$$

$$T_1 = \begin{bmatrix} \cos(\beta_1) & 0 & -\sin(\beta_1) & \left(\frac{l_{\text{joint}}}{\beta_1} \tan\left(\frac{\beta_1}{2}\right) + l_{\text{disk}} + \frac{l_{\text{joint}}}{\beta_2} \cdot \tan\left(\frac{\beta_2}{2}\right) \right) \cdot \cos(\beta_1) \\ \sin(\beta_1) & 0 & \cos(\beta_1) & \left(\frac{l_{\text{joint}}}{\beta_1} \tan\left(\frac{\beta_1}{2}\right) + l_{\text{disk}} + \frac{l_{\text{joint}}}{\beta_2} \cdot \tan\left(\frac{\beta_2}{2}\right) \right) \cdot \sin(\beta_1) \\ 0 & -1 & 0 & 0 \\ 0 & 0 & 0 & 1 \end{bmatrix} \quad (12)$$

$$T_2 = \begin{bmatrix} \cos(\beta_2) & 0 & \sin(\beta_2) & \left(l_{\text{disk}} + \frac{l_{\text{joint}}}{\beta_2} \cdot \tan\left(\frac{\beta_2}{2}\right) \right) \cdot \cos(\beta_2) \\ \sin(\beta_2) & 0 & -\cos(\beta_2) & \left(l_{\text{disk}} + \frac{l_{\text{joint}}}{\beta_2} \cdot \tan\left(\frac{\beta_2}{2}\right) \right) \cdot \sin(\beta_2) \\ 0 & 1 & 0 & 0 \\ 0 & 0 & 0 & 1 \end{bmatrix} \quad (13)$$

Then, the position and orientation of segment tip can be calculated as

$$T_0^2 = T_0 \cdot T_1 \cdot T_2 \quad (14)$$

As all segments of single section share the same construction, the forward kinematics for one section can be written in terms of bending angles of β_1 , β_2 , n, l_{joint} and l_{disk} as

$$T_{\text{section}} = (T_0^2)^n = (T_0 \cdot T_1 \cdot T_2)^n \quad (15)$$

Likewise, the forward kinematics of other sections can be obtained based on the given cable lengths. Hence, the forward kinematics for the three-section continuum robot, including the position and orientation of the tip, can be calculated as

$$T_{\text{snake}} = T_{\text{I}} \cdot T_{\text{II}} \cdot T_{\text{III}} \quad (16)$$

Inverse Kinematics (Manipulator Curvature to Cable Lengths). The purpose of inverse kinematic analysis is to determine the lengths of cables for a known position of the continuum robot tip in order to enable the operation of the robot. Because all sections share identical design, firstly the inverse kinematics of a single section is discussed.

In inverse kinematic analysis, with a given TCP, the section bending and direction angles can be derived. But closed-form expression of bending angles β_1 and β_2 , which is critical for calculating the cable lengths, can be easily obtained by the orientation angle of tip disk. As mentioned in Sec. 2, for continuum robots (flexible backbone/multi universal-joint/twin-pivot joint), section bending angle and tip disk orientation angle are not identical, as shown in Fig. 11. Therefore, an iterative method is presented for accurate inverse kinematics, which consists of two steps: Step 1: assuming the orientation of tip disk is equal with section bending angle, which is obtained from TCP, calculate β_1

and β_2 by the orientation of tip disk; Step 2: utilize β_1 and β_2 as initial approximation values and use an iteration method to compute the inverse kinematics.

Step 1. Due to the fact that the kinematics of single section depends on single segment, a kinematic model of segment is expressed for calculating β_1 and β_2 .

As shown in Fig. 12, by assuming the orientation of tip disk are equal with the bending angle of section, the bending and direction angles of segment can be written in terms of TCP position of single section (X_p , Y_p , Z_p) and n (quantity of segments in single section)

$$\begin{cases} \gamma_{\text{segment}} = \gamma_{\text{section}} = \tan^{-1}\left(\frac{Z_p}{Y_p}\right) \\ \beta_{\text{segment}} = \frac{\beta_{\text{section}}}{n} = \frac{2}{n} \cdot \tan^{-1}\left(\sqrt{\frac{Y_p^2 + Z_p^2}{X_p^2}}\right) \end{cases} \quad (17)$$

The bending angles of joint 1 and 2 in single segment can be expressed as (Appendix for detail derivation)

$$\begin{cases} \beta_1 = \tan^{-1}(\cos(\gamma_{\text{segment}}) \cdot \tan(\beta_{\text{segment}})) \\ \beta_2 = \sin^{-1}(-\sin(\gamma_{\text{segment}}) \cdot \sin(\beta_{\text{segment}})) \end{cases} \quad (18)$$

Step 2 As the actual bending angle of single section is different with tip disk orientation angle, an iteration method is presented to compute the inverse kinematics, which applies β_1 and β_2 as initial approximations, as shown in Fig. 13.

The proposed iteration method can be described as following:

Substep i. substituting β_1 and β_2 into forward kinematics equation (refer to Eq. (15)), the tip position of the section is obtained;

Substep ii. Then comparing this position with desired position, the distance differences (diff) in X, Y and Z axis (diff_x , diff_y and diff_z) are calculated;

Substep iii. comparing the distance difference $\Delta_{\text{distance}} = \sqrt{\text{diff}_x^2 + \text{diff}_y^2 + \text{diff}_z^2}$ with the desired distance error δ ;

Substep iv. if Δ_{distance} is not greater than δ , the program moves to calculate the cable lengths, based on current value of β_1 and β_2 ;

Substep v. if Δ_{distance} is greater than δ , the iteration starts. The angles β_1 and β_2 are assigned with eight combinatorial paired values that are assigned using their nominal values and Δ_β , and then the distance difference Δ_i ($i = 1-8$) are calculated, according to these eight pairs of values. Compare Δ_i and assign β_1 and β_2 new values, which obtains the minim Δ_{distance} ;

Substep vi. then repeat the procedure until the Δ_{distance} is not greater than δ .

Note: Value 1: $(\beta_1 + \Delta\beta, \beta_2)$; Value 2: $(\beta_1 + \Delta\beta, \beta_2 + \Delta\beta)$; Value 3: $(\beta_1 + \Delta\beta, \beta_2 - \Delta\beta)$; Value 4: $(\beta_1 - \Delta\beta, \beta_2)$; Value 5: $(\beta_1 - \Delta\beta, \beta_2 + \Delta\beta)$; Value 6: $(\beta_1 - \Delta\beta, \beta_2 + \Delta\beta)$; Value 7: $(\beta_1, \beta_2 + \Delta\beta)$; Value 8: $(\beta_1, \beta_2 - \Delta\beta)$;

Based on the angle values of β_1 and β_2 obtained from the iteration program, cable lengths l'_1, l'_2, l'_3 and l'_4 in gap 1 can be written as, as shown in Fig. 8

$$\left\{ \begin{array}{l} l'_1 = 2 \cdot \left(\frac{l_{\text{joint}}}{\beta_1} - r \cdot \sin(\theta_1) \right) \cdot \tan\left(\frac{\beta_1}{2}\right) \\ l'_2 = 2 \cdot \left(\frac{l_{\text{joint}}}{\beta_1} - r \cdot \cos(\theta_1) \right) \cdot \tan\left(\frac{\beta_1}{2}\right) \\ l'_3 = 2 \cdot \left(\frac{l_{\text{joint}}}{\beta_1} + r \cdot \sin(\theta_1) \right) \cdot \tan\left(\frac{\beta_1}{2}\right) \\ l'_4 = 2 \cdot \left(\frac{l_{\text{joint}}}{\beta_1} + r \cdot \cos(\theta_1) \right) \cdot \tan\left(\frac{\beta_1}{2}\right) \end{array} \right. \quad (19)$$

Similarly, cable lengths l''_1, l''_2, l''_3 and l''_4 in gap 2 can be described as

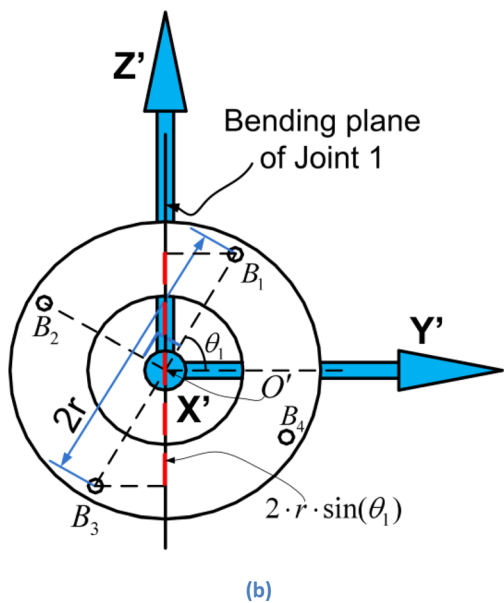
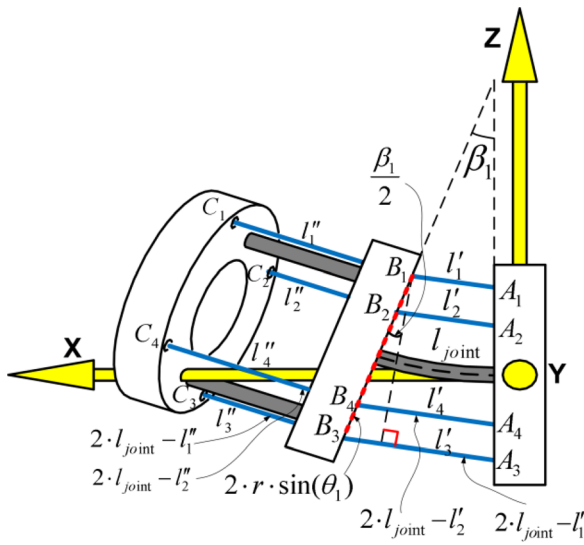


Fig. 9 (a) Joint 1 bending section view (b) Top view of disk B

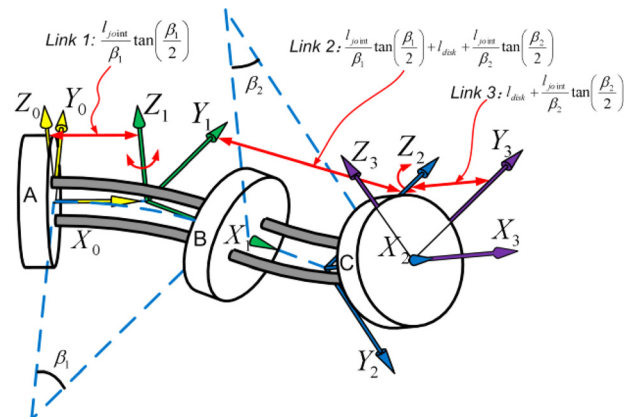


Fig. 10 DH frames for one single segment (Coordinate 0 and 3 locate at the center of the top surface of the disks A and C; Coordinate 1 locates at the intersection point of central axes of disks A and B; Coordinate 2 locates at the intersection point of central axes of disks B and C; bending plane β_1 is vertical with bending plane β_2)

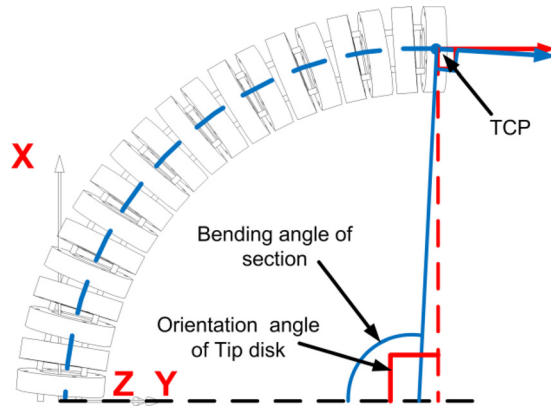


Fig. 11 Difference between section bending angle and tip disk orientation (twin-pivot backbone continuum robot)

$$\left\{ \begin{array}{l} l''_1 = 2 \cdot \left(\frac{l_{\text{joint}}}{\beta_2} - r \cdot \cos(\theta_1) \right) \cdot \tan\left(\frac{\beta_2}{2}\right) \\ l''_2 = 2 \cdot \left(\frac{l_{\text{joint}}}{\beta_2} - r \cdot \sin(\theta_1) \right) \cdot \tan\left(\frac{\beta_2}{2}\right) \\ l''_3 = 2 \cdot \left(\frac{l_{\text{joint}}}{\beta_2} + r \cdot \cos(\theta_1) \right) \cdot \tan\left(\frac{\beta_2}{2}\right) \\ l''_4 = 2 \cdot \left(\frac{l_{\text{joint}}}{\beta_2} + r \cdot \sin(\theta_1) \right) \cdot \tan\left(\frac{\beta_2}{2}\right) \end{array} \right. \quad (20)$$

Therefore, according to Eqs. (19) and (20), the inverse kinematics for single section (determine the lengths of cables for a known position of the robot tip) can be calculated as

Table 1 D-H parameters for single segment

Link	θ	a	d	α
1	0	$\frac{l_{\text{joint}}}{\beta_1} \tan\left(\frac{\beta_1}{2}\right)$	0	0
2	β_1	$\frac{l_{\text{joint}}}{\beta_1} \tan\left(\frac{\beta_1}{2}\right) + l_{\text{disk}} + \frac{l_{\text{joint}}}{\beta_2} \cdot \tan\left(\frac{\beta_2}{2}\right)$	0	$-\frac{\pi}{2}$
3	β_2	$l_{\text{disk}} + \frac{l_{\text{joint}}}{\beta_2} \cdot \tan\left(\frac{\beta_2}{2}\right)$	0	$\frac{\pi}{2}$

$$\begin{cases} l_1 = 2n \cdot \left(\frac{l_{\text{joint}}}{\beta_1} - r \cdot \sin(\theta_1) \right) \cdot \tan\left(\frac{\beta_1}{2}\right) + 2n \cdot \left(\frac{l_{\text{joint}}}{\beta_2} - r \cdot \cos(\theta_1) \right) \cdot \tan\left(\frac{\beta_2}{2}\right) \\ l_2 = 2n \cdot \left(\frac{l_{\text{joint}}}{\beta_1} - r \cdot \cos(\theta_1) \right) \cdot \tan\left(\frac{\beta_1}{2}\right) + 2n \cdot \left(\frac{l_{\text{joint}}}{\beta_2} - r \cdot \sin(\theta_1) \right) \cdot \tan\left(\frac{\beta_2}{2}\right) \\ l_3 = 2n \cdot \left(\frac{l_{\text{joint}}}{\beta_1} + r \cdot \sin(\theta_1) \right) \cdot \tan\left(\frac{\beta_1}{2}\right) + 2n \cdot \left(\frac{l_{\text{joint}}}{\beta_2} + r \cdot \cos(\theta_1) \right) \cdot \tan\left(\frac{\beta_2}{2}\right) \\ l_4 = 2n \cdot \left(\frac{l_{\text{joint}}}{\beta_1} + r \cdot \cos(\theta_1) \right) \cdot \tan\left(\frac{\beta_1}{2}\right) + 2n \cdot \left(\frac{l_{\text{joint}}}{\beta_2} + r \cdot \sin(\theta_1) \right) \cdot \tan\left(\frac{\beta_2}{2}\right) \end{cases} \quad (21)$$

Cable Tension Analysis. The purpose of this section is verifying if the tension of the pair of actuation cable can be maintained at constant value in arbitrary configuration, based on the proposed construction. There are several factors affecting the cable tension, including the bend of the continuum robot, spool rotation, geometric tolerance of constitutive elements and control system. Due to that the spool rotation can feed in and pull out the same cable lengths from both sides, in this paper, the bend of continuum robot is assumed to be the main source of cable tension change. By comparing the gap distance $A_iB_i + B_iC_i$ ($i = 1, 2, 3, 4$) with the original total cable length of one pair of cables, the tension condition can be obtained [27].

Referring to Fig. 8, the gap distances for cable l'_1 and l'_3 in gap 1 can be calculated as

$$\begin{cases} A_1B_1 = 2 \cdot \left(\frac{l_{\text{joint}}}{\beta_1} - r \cdot \sin(\theta_1) \right) \cdot \sin\left(\frac{\beta_1}{2}\right) \\ A_3B_3 = 2 \cdot \left(\frac{l_{\text{joint}}}{\beta_1} + r \cdot \sin(\theta_1) \right) \cdot \sin\left(\frac{\beta_1}{2}\right) \end{cases} \quad (22)$$

And likewise, the gap distances for cable l''_1 and l''_3 in gap 2 can be expressed as

$$\begin{cases} B_1C_1 = 2 \cdot \left(\frac{l_{\text{joint}}}{\beta_2} - r \cdot \cos(\theta_1) \right) \cdot \sin\left(\frac{\beta_2}{2}\right) \\ B_3C_3 = 2 \cdot \left(\frac{l_{\text{joint}}}{\beta_2} + r \cdot \cos(\theta_1) \right) \cdot \sin\left(\frac{\beta_2}{2}\right) \end{cases} \quad (23)$$

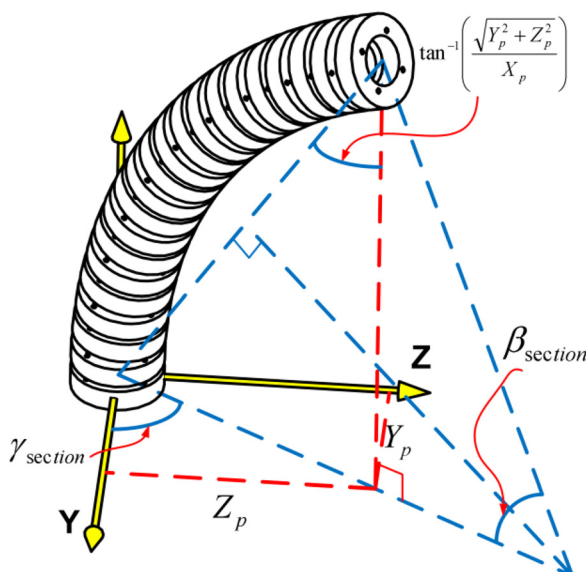


Fig. 12 Configuration of single section

Therefore, the gap distance in one section for one pair of cables can be written as

$$\begin{aligned} l_{\text{gap}} &= n \cdot \sum_{i=1,3} (A_iB_i + B_iC_i) \\ &= 2 \cdot n \cdot l_{\text{joint}} \left(\frac{\sin(\beta_1/2)}{\beta_1} + \frac{\sin(\beta_2/2)}{\beta_2} \right) \end{aligned} \quad (24)$$

Hence, the cable tension force can be obtained as

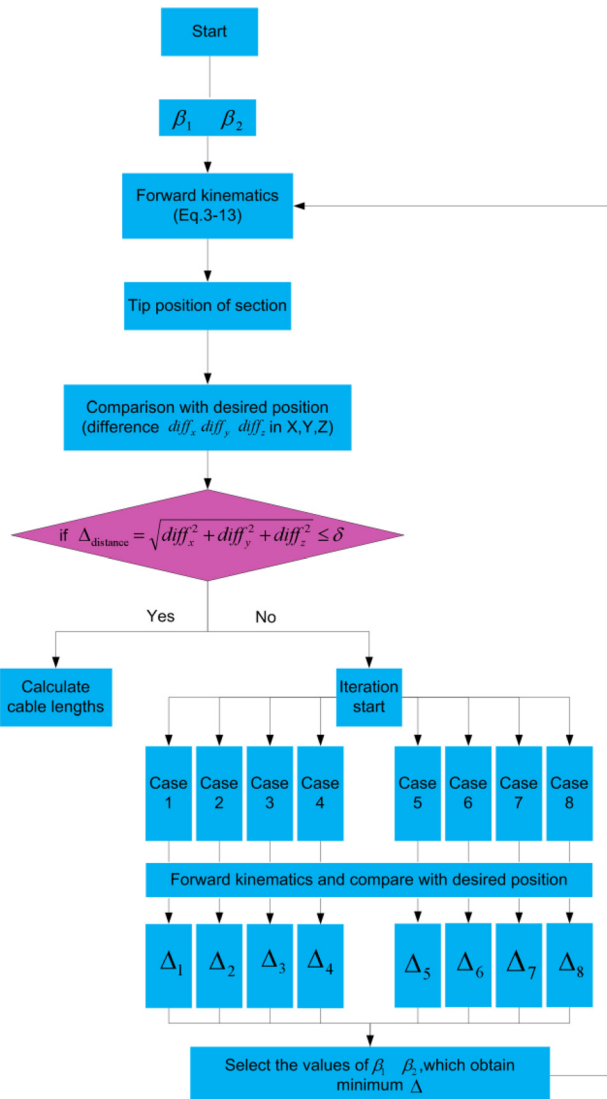


Fig. 13 Iteration method for inverse kinematics

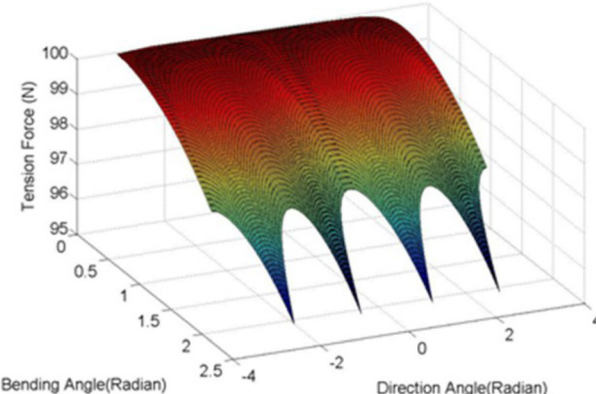


Fig. 14 An example of cable tension plot in work volume of single section (stiffness $k = 37.5 \text{ N/mm}$ of a 0.75 mm diameter steel cable of 400 mm length; 200 mm in continuum unit and 200 mm in actuation system); in the work volume, the original tension is 100 N at 0 deg bending; the min tension is 95 N at bending angle 131.8 deg, direction angle ± 46.4 deg and ± 133.5 deg

$$F = F_{\text{original}} + K_{\text{cable}} \cdot (l_{\text{gap}} - l_{\text{original}}) \quad (25)$$

Figure 14 shows a case study of the cable tension in the work volume. Let the pretension of cable be 100 N at the original position (bending angle is 0 deg). In the work volume, the tension force modifies when the continuum robot bends, and the minimum tension force is 95 N, when the section bends 131.8 deg at direction angle ± 46.4 deg and ± 133.5 deg. Therefore, the cable tension can be maintained in any arbitrary configuration, which remains at least 95% of original tension. Based on this fact, twin actuation is applied in the design, which eliminates the weight and size of actuation system.

Work Volume Analysis. For performing 3D movements (e.g., machining, inspection) with the continuum robot, the evaluation of the work volume is critical. This section addresses the problem of determining the region reachable by the tip of the continuum robot. The max bending angle of single joint is evaluated, and then the work volume of single section and the system (three sections) are analyzed to calculate the work volume.

Max bending angle of single joint:

In the proposed system, the max bending angle of single joint (θ_{\max}) depends on two factors: (1) yield of the joint material caused by bending; (2) geometry limitation.

Firstly, the motion range is discussed in terms of yield of the joint material caused by bending. Super-elastic NiTi has greater recoverable elastic strain ($\sim 8\%$) than other alloys (e.g., stainless steel: approximately 0.5%) [28], hence, it is employed as compliant joints in the system.

As shown in Fig. 15, the strain of joint can be expressed as

$$\text{Strain}_{\text{edge}} = \frac{\Delta l_{\text{joint}}}{l_{\text{joint}}} = \frac{\left(\frac{l_{\text{joint}}}{\theta} + \frac{d}{2} \right) \cdot \theta - l_{\text{joint}}}{l_{\text{joint}}} = \frac{\frac{d}{2} \cdot \theta}{l_{\text{joint}}} = \frac{d \cdot \theta}{2 \cdot l_{\text{joint}}} \quad (26)$$

Where d is the diameter of super-elastic NiTi joint. Based on Eq. (26), strain for different bending angles is calculated and shown in Table 2.

Secondly, the other factor, geometry limitation is presented. Specifically, the motion range depends on the max bending angle when the adjacent disks have collision. The bending radius is described as

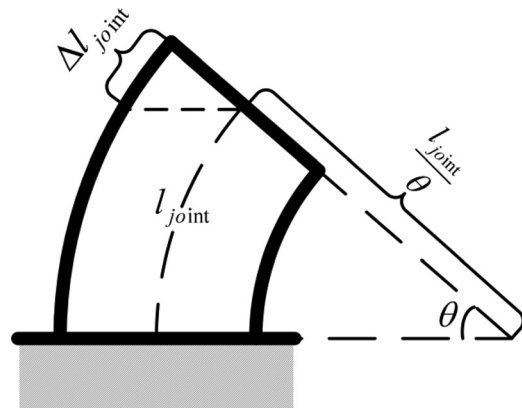


Fig. 15 Strain model of single compliant joint

$$R_{\text{bending}} = \frac{l_{\text{joint}}}{\theta} \quad (27)$$

When the bending radius is equal to the radius of the disk, the disk collides with the adjacent one and the joint gets the max bend, as shown in Fig. 16.

Hence, the max bending angle is expressed as

$$\theta_{\max} = \frac{l_{\text{joint}}}{R_{\text{disk}}} = \frac{1.5}{7.5} = 11.46 \text{ deg} \quad (28)$$

Therefore, based on the design presented in this paper, one joint can bend up to 11.46 deg by employing 1.5 mm long, Ø1 super-elastic rod as compliant joint.

Work Volume of the System. Based on the single-joint max bending range, the work volume of single section is presented. For avoiding the collision between the adjacent disks, single joint is allowed to be bent up to 9 deg, and then the points on the work volume is calculated by an algorithm, which is based on forward kinematics. As shown in Fig. 17(a), it can be found that single section can bend at least 90 deg in arbitrary direction. Likewise, the work volume of three-section continuum robot is obtained in Fig. 17(b).

Experimental Validation

For demonstration purpose, a three-section prototype is built, which is specifically described in Sec. 3. For validating the kinematics model, the TCP positions of the continuum robot system are measured by video gauge system, as shown in Fig. 18. Further, for validating the design concept, the twisting angle is measured at different configurations, when the robot operates in the horizontal plane. And load carrying capability of the system is also tested, by applying different pay loads at the tip of the arm.

Accuracy and Motion Range of Multisection Continuum Robot. Figure 19 shows several snapshots of motion of the three sections manipulator system prototype. As shown in Figs. 19(a)–19(d), single section sends to 90 deg in different directions. Figure 19(e) illustrates multiple section bending.

As shown in Table 3, the position accuracy error of the system is less than 1 mm in translation for sweeping in any operation area (the operation principle: after the continuum robot reaches the desired area, the tip section will be utilized to operate in the confined space with an end effector. As shown in Fig. 20, ± 5 deg movement from original position where TCP researches the operation area is required for this operation). This error can be minimized by applying a shape sensor in the continuum unit, which is the research for next step.

Table 2 Strain of NiTi compliant joint against angles

Max. bending angle of single joint	9 deg	12 deg	Note
Strain	5.24%	6.98%	1 mm diameter; 1.5 mm long.

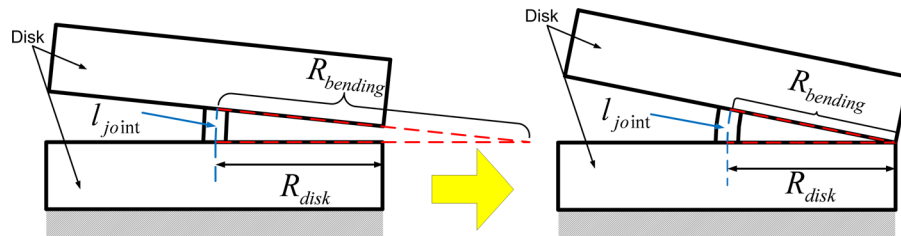


Fig. 16 Max bending of one joint

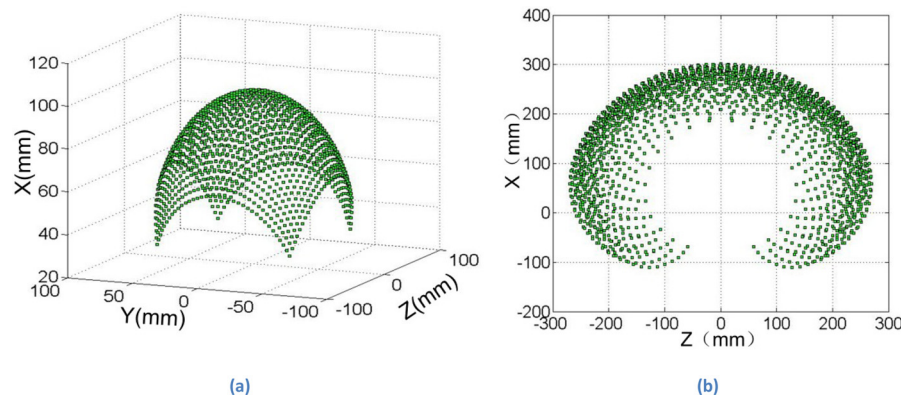


Fig. 17 Work volume (a) 3D single section work volume and (b) 2D section view of three sections work volume (XZ)

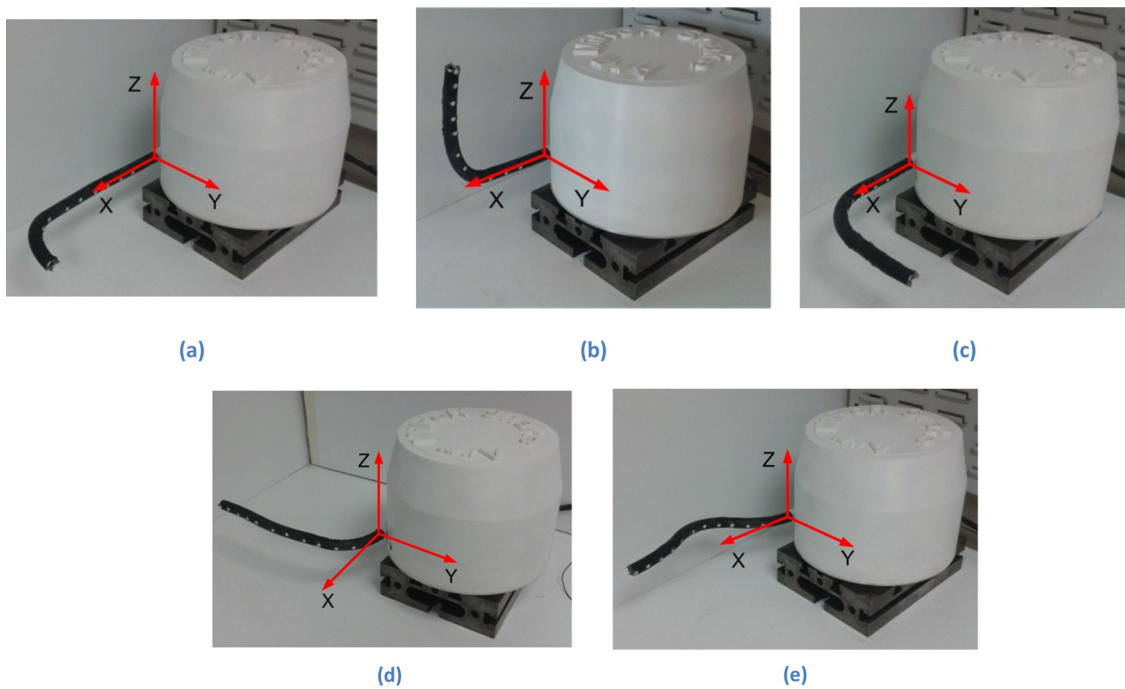


Fig. 18 Three-section continuum demonstrator performing controlled motions

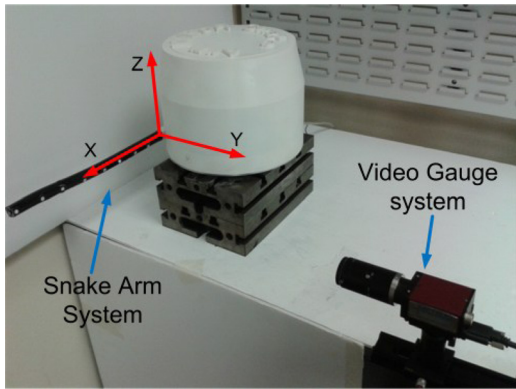


Fig. 19 The setup of the measurement system (IMETRUM video gauge system)

Table 3 Position accuracy measurement results

Bending angle (deg)	Desired position		Actual position		Error	
	X	Z	X	Z	ΔX	Z
25	40.41	104.23	40.51	104.1	0.1	-0.13
27	41.19	102.1	41.25	102.09	0.06	-0.01
29	41.97	99.97	41.98	100.04	0.01	0.07
31	42.75	97.91	42.76	97.95	0.01	0.04
33	43.53	95.78	43.58	95.79	0.05	0.01
35	44.31	93.65	44.46	93.77	0.15	0.12
Original position:						
$\beta_{\text{section_III}} = 30 \text{ deg}$, $\beta_{\text{section_II}} = 0 \text{ deg}$, $\beta_{\text{section_I}} = 0 \text{ deg}$;						
$\gamma_{\text{section_I}} = \gamma_{\text{section_II}} = \gamma_{\text{section_III}} = 90 \text{ deg}$						
40	46.63	88.6	46.89	88.75	0.26	0.15
42	47.88	86.47	47.92	86.78	0.04	0.31
44	49.13	84.34	49.02	84.61	-0.11	0.27
46	50.37	82.2	49.78	83.2	-0.59	1
48	51.62	80.07	50.96	80.89	-0.66	0.82
50	52.87	77.94	52.9	77.2	0.03	-0.74
Original position:						
$\beta_{\text{section_III}} = 45 \text{ deg}$, $\beta_{\text{section_II}} = 0 \text{ deg}$, $\beta_{\text{section_I}} = 0 \text{ deg}$;						
$\gamma_{\text{section_I}} = \gamma_{\text{section_II}} = \gamma_{\text{section_III}} = 90 \text{ deg}$						
55	55.92	71.67	56.35	71.55	0.43	-0.12
57	57.64	69.54	57.92	69.38	0.28	-0.16
59	59.35	67.41	59.39	67.42	0.04	0.01
61	61.07	65.27	60.85	65.5	-0.22	0.23
63	62.78	63.14	62.45	63.68	-0.33	0.54
65	64.5	61.01	64.04	62.01	-0.46	1
Original position:						
$\beta_{\text{section_III}} = 60 \text{ deg}$, $\beta_{\text{section_II}} = 0 \text{ deg}$, $\beta_{\text{section_I}} = 0 \text{ deg}$;						
$\gamma_{\text{section_I}} = \gamma_{\text{section_II}} = \gamma_{\text{section_III}} = 90 \text{ deg}$						

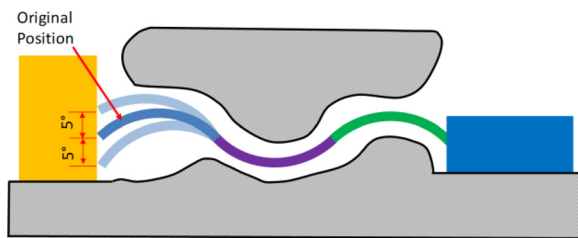
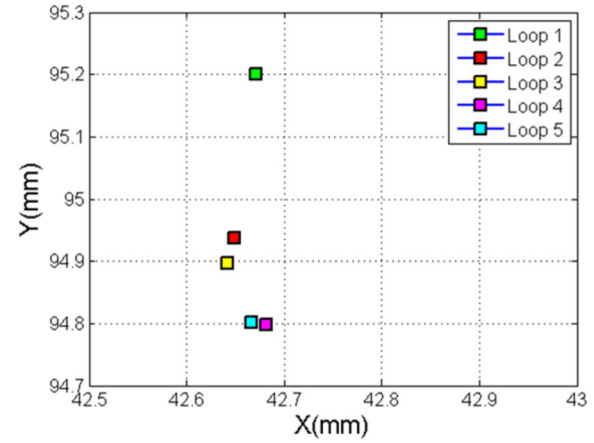
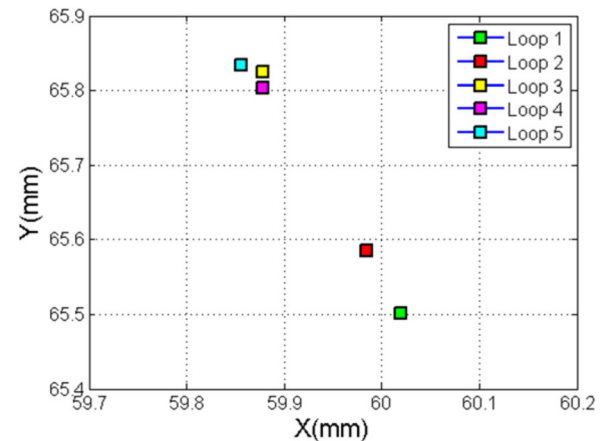


Fig. 20 Operation approach for the system

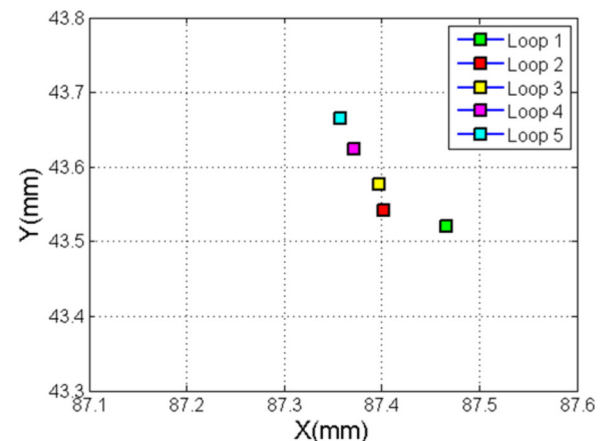
The repeatability of the demonstrator measured by video gauge system is presented in Fig. 21. The continuum robot is driven to bend from 0 deg to 90 deg (60 deg and 30 deg) and back 0 deg for five loops, in order to measure the repeatability of the system. The



(a)



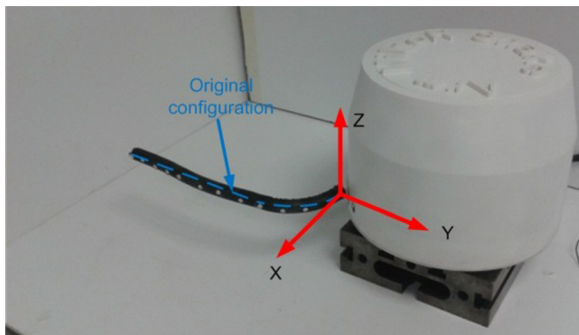
(b)



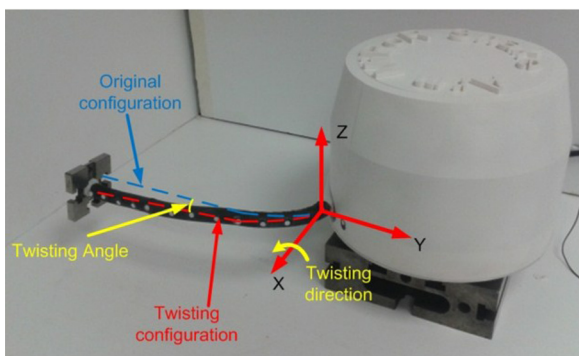
(c)

Fig. 21 Repeatability of three-section demonstrator: (a): TCP position repeatability test with respect to 30 deg bend (b):TCP position repeatability test with respect to 60 deg bend (c):TCP position repeatability test with respect to 90 deg bend (Note: One bend and return is called one loop)

repeatability error of system is less than 0.5 mm in the work volume, as shown in Figs. 21(a)-21(c). The small repeatability error also proves the tension of all the cables is kept well in the work volume of the system. Note: all these measurements for



(a)



(b)

Fig. 22 Twisting measurement of three-section demonstrator: configuration for twisting measurement (a) original configuration without end load (b) twisting configuration

repeatability are made at configurations of middle and base sections: 0 deg bend, direction angle: 0 deg.

Twisting Angle Measurement and Load Carrying Capability of the System. In this paper, the main emphasis on the design aspect is given to minimize the twisting problem of the continuum unit. As the max moment can be generated, when the base section bends 90 deg in horizontal plane, thus, the twisting angle of the continuum robot is measured at the configuration shown in Fig. 22. At this configuration, the twisting angle of base section is 0.61 deg and 1.33 deg, respect to 200 g and 450 g end load applied at the tip of the system, respectively. Compared with central located flexible backbone continuum robot, the twisting angle of our system is really small and can be ignored.

Figure 23 illustrates the several snapshots of motion of the manipulator system prototype carrying an end load (200 g and 450 g).

Conclusion

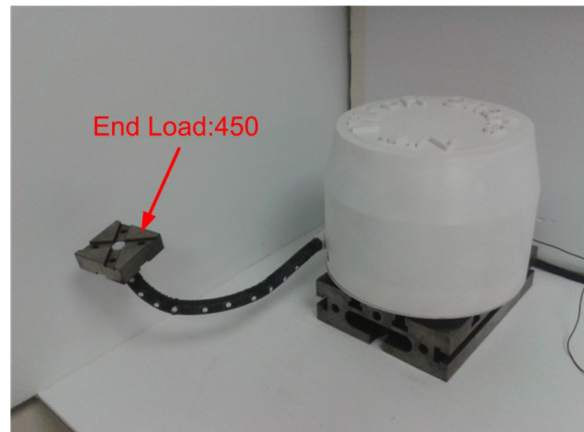
In this paper, a new continuum robot is introduced, which is different from other continuum robots in twin-pivot compliant joint design. The advantages residing from this design can be summarized as:

- High flexibility (90 deg bend for each section), small diameter/length ratio (15 mm/280 mm) and an appropriate stiffness enabled by compliant joint construction.
- Minimized twisting angle enabled by twin-pivot construction.

Based on this concept, an accurate kinematic model for this novel construction is introduced. To support this, the cable length in arbitrary configuration is also calculated for verifying the tension maintenance. According to this calculation, the cables can



(a)



(b)

Fig. 23 Three-section demonstrator performing load carrying capability: (a) 200 g end load and (b) 450 g end load

maintain at least 95% of original tension force at arbitrary configuration, when the continuum robot bends.

Finally, for validating the design, kinematics and work volume analyses, a three-section demonstrator is developed. In the work volume of the system, the position control error is less than 1 mm in translation in operation area. And the max repeatability error is less than 0.5 mm in the work volume. The twisting angles are 0.61 deg and 1.33 deg with respect to different end loads, 200 g and 450 g, respectively, (measured in the worst scenario: 90 deg bend in base section in horizontal plane, respectively). Furthermore, the proposed continuum robot presents a relatively large payload (200 g and 450 g) can be carried at the tip, so the system is capable to take diverse end effectors for a variety of applications.

For the future research, more precise position control needs to be developed for minimizing the control error by assisting a shape sensor, which can feed back the actual shape of the system. Furthermore, based on the design and kinematic model presented in this paper, stiffness matrix and deflection compensation approach needs to be developed, due to the error/deflection caused by end load.

Acknowledgment

The authors thank Mr. David Palmer and Stuart Branston for their supports on system design, manufacturing and testing of this demonstrator.

The research leading to these results has received funding from the European Union Seventh Framework Programme (FP7/2011)

under Grant Agreement No. 284959 (MiRoR) and the Dorothy Hodgkin Scholarship from EPSRC UK.

Nomenclature

- A_i = guide points for the cables on the disk A, $i = 1, 2, 3, 4$
- B_i = guide points for the cables on the disk B, $i = 1, 2, 3, 4$
- C_i = anchor points for the cables on the disk C, $i = 1, 2, 3, 4$
- F_{original} = original cable tension force
- K_{cable} = stiffness of cable
- l_{disk} = thickness of the disks (given)
- l_{gap} = gap distance for one pair of cables in one section
- l_{joint} = length of the compliant joints (given)
- l_{original} = original length of one pair of cables in one section
- l_1, l_2 = total lengths of cables 1 and 2, respectively (given)
- l'_1, l''_1 = lengths of cable 1 in gaps 1 and 2, respectively
- l'_2, l''_2 = lengths of cable 2 in gaps 1 and 2, respectively
- l'_3, l''_3 = lengths of cable 3 in gaps 1 and 2, respectively
- l'_4, l''_4 = lengths of cable 4 in gaps 1 and 2, respectively
- N = quantity of segments in single section (given)
- R = distance from center of the disk to the cable anchor point (given)
- XYZ = coordinate system located at the center of disks A
- $X'Y'Z'$ = coordinate system located at the center of disks B
- $X''Y''Z''$ = coordinate system located at the center of disks C
- (X_p, Y_p, Z_p) = The tip position of single section
- β_{segment} = Bending angle of segment
- β_{section} = Bending angle of section
- β_1 = bending angle of joint_1
- β_2 = bending angle of joint_2
- γ_{segment} = Direction angle of segment
- γ_{section} = Direction angle of section
- θ_1 = angle between B_1B_3 and axis Y' (given, as shown in Fig. 8(b))

Appendix: The Derivation of Eqs. (3)–(16)

As shown in Fig. 9, based on Table II (D–H parameters for single segment), the orientation of disk B and C (R_1 and R_2) with respect to coordinates XYZ and $X'Y'Z'$ can be obtained as

$$R_1 = \begin{bmatrix} \cos(\beta_1) & -\sin(\beta_1) & 0 \\ \sin(\beta_1) & \cos(\beta_1) & 0 \\ 0 & 0 & 1 \end{bmatrix} \quad (\text{A1})$$

$$R_2 = \begin{bmatrix} \cos(\beta_2) & 0 & \sin(\beta_2) \\ 0 & 1 & 0 \\ -\sin(\beta_2) & 0 & \cos(\beta_2) \end{bmatrix} \quad (\text{A2})$$

Therefore, the orientation of disk C (R_C) with respect to coordinate XYZ can be expressed as

$$R_C = R_1 \cdot R_2 = \begin{bmatrix} R_{11} & R_{12} & R_{13} \\ R_{21} & R_{22} & R_{23} \\ R_{31} & R_{32} & R_{33} \end{bmatrix} \quad (\text{A3})$$

Where $R_{11} = \cos(\beta_1)\cos(\beta_2)$; $R_{12} = -\sin(\beta_1)$; $R_{13} = \cos(\beta_1)\sin(\beta_2)$; $R_{21} = \cos(\beta_2)\sin(\beta_1)$; $R_{22} = \cos(\beta_1)R_{23} = \sin(\beta_1)\sin(\beta_2)$; $R_{31} = -\sin(\beta_2)$; $R_{32} = 0$; $R_{33} = \cos(\beta_2)$.

The orientation of disk C can be also written in terms of bending and direction angle of this segment as [27]

$$R_C = \begin{bmatrix} R'_{11} & R'_{12} & R'_{13} \\ R'_{21} & R'_{22} & R'_{23} \\ R'_{31} & R'_{32} & R'_{33} \end{bmatrix} \quad (\text{A4})$$

Where $R'_{11} = \cos(\beta_{\text{segment}})$; $R'_{12} = -\cos(\gamma_{\text{segment}}) \cdot \sin(\beta_{\text{segment}})$; $R'_{13} = -\sin(\gamma_{\text{segment}}) \cdot \sin(\beta_{\text{segment}})$; $R'_{21} = \cos(\gamma_{\text{segment}}) \cdot \sin(\beta_{\text{segment}})$; $R'_{22} = \cos(\beta_{\text{segment}}) - \sin(\gamma_{\text{segment}})^2$; $(\cos(\beta_{\text{segment}}) - 1)R'_{23} = \cos(\gamma_{\text{segment}}) \cdot \sin(\gamma_{\text{segment}}) \cdot (\cos(\beta_{\text{segment}}) - 1)$; $R'_{31} = \sin(\gamma_{\text{segment}}) \cdot \sin(\beta_{\text{segment}})$; $R'_{32} = \cos(\gamma_{\text{segment}}) \cdot \sin(\gamma_{\text{segment}}) \cdot (\cos(\beta_{\text{segment}}) - 1)$; $R'_{33} = \cos(\beta_{\text{segment}}) - \cos(\gamma_{\text{segment}})^2 \cdot (\cos(\beta_{\text{segment}}) - 1)$.

Hence, the following relationship can be obtained

$$\begin{cases} \frac{R_{11}}{R_{21}} = \frac{R'_{11}}{R'_{21}} \\ R_{31} = R'_{31} \end{cases} \quad (\text{A5})$$

Therefore, according to Eq. (A5), Eq. (18) can be derived.

References

- [1] Asari, V. K., Kumar, S., and Kassim, I. M., 2000, "A Fully Autonomous Micro-robotic Endoscopy System," *J. Intell. Rob. Syst.*, **28**(4), pp. 325–341.
- [2] Bailly, Y., Amirat, Y., and Fried, G., 2011, "Modeling and Control of a Continuum Style Microrobot for Endovascular Surgery," *IEEE Trans. Rob.*, **27**(5), pp. 1024–1030.
- [3] Hu, H., Wang, P., Zhao, B., Li, M., and Sun, L., 2009, "Design of a Novel Snake-Like Robotic Colonoscope," IEEE International Conference on Robotics and Biomimetics (ROBIO), Guilin, China, Dec. 19–23, pp. 1957–1961.
- [4] Kim, Y.-J., Cheng, S., Kim, S., and Iagnemma, K., 2014, "A Stiffness-Adjustable Hyperredundant Manipulator Using a Variable Neutral-Line Mechanism for Minimally Invasive Surgery," *IEEE Trans. Rob.*, **30**(2), pp. 382–395.
- [5] Simaan, N., 2005, "Snake-Like Units Using Flexible Backbones and Actuation Redundancy for Enhanced Miniaturization," IEEE International Conference on Robotics and Automation (ICRA), Barcelona, Spain, Apr. 18–22, pp. 3012–3017.
- [6] Simaan, N., Taylor, R., and Flint, P., 2004, "A Dexterous System for Laryngeal Surgery," IEEE International Conference on Robotics and Automation (ICRA'04), New Orleans, LA, Apr. 26–May 1, pp. 351–357.
- [7] Webster, R. J., Romano, J. M., and Cowan, N. J., 2009, "Mechanics of Precurved-Tube Continuum Robots," *IEEE Trans. Rob.*, **25**(1), pp. 67–78.
- [8] Yoon, H.-S., and Yi, B.-J., 2009, "A 4-DOF Flexible Continuum Robot Using a Spring Backbone," International Conference on Mechatronics and Automation (ICMA 2009), Changchun, China, Aug. 9–12, pp. 1249–1254.
- [9] Chen, G., Fu, L. M., Pham, T., and Redarce, T., 2013, "Characterization and Modeling of Pneumatic Actuator for a Soft Continuum Robot," IEEE International Conference on Mechatronics and Automation (ICMA), Takamatsu, Japan, Aug. 4–7, pp. 243–248.
- [10] Gravagne, I. A., and Walker, I. D., 2000, "On the Kinematics of Remotely-Actuated Continuum Robots," IEEE International Conference on Robotics and Automation (ICRA'00), San Francisco, CA, Apr. 24–28, pp. 2544–2550.
- [11] Shamma, E., Wolf, A., and Choset, H., 2006, "Three Degrees-of-Freedom Joint for Spatial Hyper-Redundant Robots," *Mech. Mach. Theory*, **41**(2), pp. 170–190.
- [12] Ohno, H., and Hirose, S., 2001, "Design of Slim Slime Robot and Its Gait of Locomotion," IEEE/RSJ International Conference on Intelligent Robots and Systems (IROS), Maui, HI, Oct. 29–Nov. 3, pp. 707–715.
- [13] OC Robotics, 2008, "Snake-Arm Robots Access the Inaccessible," *Nucl. Technol. Int.*, **1**, pp. 92–94.
- [14] OC Robotics, 2015, "Snake-Arm Robots for Aircraft Assembly," OC Robotics, Bristol, UK, <http://www.ocrobotics.com/applications-solutions/aerospace/aerospace-case-study/>
- [15] Chen, Y., Liang, J., and Hunter, I. W., 2014, "Modular Continuum Robotic Endoscope Design and Path Planning," IEEE International Conference on Robotics and Automation (ICRA), Hong Kong, May 31–June 7, pp. 5393–5400.
- [16] Walker, I. D., and Hannan, M. W., 1999, "A Novel 'Elephant's Trunk' Robot," IEEE/ASME International Conference on Advanced Intelligent Mechatronics (AIM), Atlanta, GA, Sept. 19–23, pp. 410–415.
- [17] Simaan, N., Xu, K., Wei, W., Kapoor, A., Kazanzides, P., Taylor, R., and Flint, P., 2009, "Design and Integration of a Telerobotic System for Minimally Invasive Surgery of the Throat," *Int. J. Rob. Res.*, **28**(9), pp. 1134–1153.
- [18] Walker, I. D., 2013, "Continuous Backbone 'Continuum' Robot Manipulators," *ISRN Rob.*, **2013**, p. 726506.
- [19] Qi, P., Qiu, C., Liu, H., Dai, J. S., Seneviratne, L., and Althoefer, K., 2014, "A Novel Continuum-Style Robot With Multilayer Compliant Modules," IEEE/RSJ International Conference on Intelligent Robots and Systems (IROS 2014), Chicago, IL, Sept. 14–18, pp. 3175–3180.
- [20] Murphy, R. J., Otake, Y., Taylor, R. H., and Armand, M., 2014, "Predicting Kinematic Configuration From String Length for a Snake-Like Manipulator not

- Exhibiting Constant Curvature Bending," IEEE/RSJ International Conference on Intelligent Robots and Systems (**IROS 2014**), Chicago, IL, Sept. 14–18, pp. 3515–3521.
- [21] Jones, B. A., and Walker, I. D., 2006, "Practical Kinematics for Real-Time Implementation of Continuum Robots," *IEEE Trans. Rob.*, **22**(6), pp. 1087–1099.
- [22] Jones, B. A., and Walker, I. D., 2006, "Kinematics for Multisection Continuum Robots," *IEEE Trans. Rob.*, **22**(1), pp. 43–55.
- [23] Xu, K., and Simaan, N., 2010, "Analytic Formulation for Kinematics, Statics, and Shape Restoration of Multibackbone Continuum Robots Via Elliptic Integrals," *J. Mech. Rob.*, **2**(1), p. 011006.
- [24] Webster, R. J., and Jones, B. A., 2010, "Design and Kinematic Modeling of Constant Curvature Continuum Robots: A Review," *Int. J. Rob. Res.*, **29**(13), pp. 1661–1683.
- [25] McMahan, W., Jones, B. A., and Walker, I. D., 2005, "Design and Implementation of a Multi-Section Continuum Robot: Air-Octopus," IEEE/RSJ International Conference on Intelligent Robots and Systems (**IROS 2005**), Edmonton, Canada, Aug. 2–6, pp. 2578–2585.
- [26] Hannan, M., and Walker, I., 2001, "The 'Elephant Trunk' Manipulator, Design and Implementation," IEEE/ASME International Conference on Advanced Intelligent Mechatronics (**AIM**), Como, Italy, July 8–12, pp. 14–19.
- [27] Dong, X., Raffles, M., Guzman, S. C., Axinte, D., and Kell, J., 2014, "Design and Analysis of a Family of Snake Arm Robots Connected by Compliant Joints," *Mech. Mach. Theory*, **77**, pp. 73–91.
- [28] McKelvey, A., and Ritchie, R., 1999, "Fatigue-Crack Propagation in Nitinol, a Shape-Memory and Superelastic Endovascular Stent Material," *J. Biomed. Mater. Res.*, **47**(3), pp. 301–308.